THE JOURNAL OF NAVIGATION (2014), **67**, 753–775. © The Royal Institute of Navigation 2014
doi:10.1017/S0373463314000241

Bayesian Fault-Tolerant Position Estimator and Integrity Risk Bound for GNSS Navigation

Fang-Cheng Chan, Mathieu Joerger, Samer Khanafseh and Boris Pervan

(*Illinois Institute of Technology*)
(E-mail: chanfan@iit.edu)

The advent of multiple Global Navigation Satellite System (GNSS) constellations will result in a considerable increase in the number of satellites for positioning worldwide. This substantial improvement in measurement redundancy has the potential to radically advance receiver autonomous integrity monitoring (RAIM) performance. However, regardless of the number of satellites, the performance of existing RAIM methods is sensitive to the assumed prior probabilities of individual fault hypotheses. In this paper, a new method is developed using Bayes' theorem to generate upper bounds on *posterior* probabilities of individual fault hypotheses given current user measurements. These bounds are used in a Bayesian fault-tolerant position estimator (FTE) that minimizes integrity risk. The detection test statistic is a measurement-based integrity risk bound, which is directly compared with a pre-specified risk requirement. The associated challenge of quantifying continuity risk is resolved using a bounding approach, which is also detailed in this work. The new Bayesian FTE method is shown to be more robust to uncertainty in prior probability of fault occurrence than existing RAIM methods.

KEYWORDS

1. Global Navigation Satellite Systems (GNSS). 2. Bayesian probability. 3. Fault-tolerance position estimation. 4. RAIM. 5. Navigation integrity.

Submitted: 4 October 2013. Accepted: 23 March 2014. First published online: 17 April 2014.

1. INTRODUCTION.

Multiple Global Navigation Satellite System (GNSS) constellations, including the Global Positioning System (GPS), GLONASS, Galileo and BeiDou are currently being deployed or modernised, and are foreseen to be fully operational in the 2020–2030 time frame. The completed, combined multi-constellation GNSS will broadcast new signals from a large number of additional ranging sources, and is therefore expected to provide improved positioning performance. In particular, the abundantly redundant range measurements available using multi-constellation GNSS can significantly increase the performance of receiver autonomous integrity monitoring (RAIM) (Parkinson and Axelrad, 1988; Brown, 1996). This potential performance improvement has raised a renewed interest in using

https://doi.org/10.1017/S0373463314000241 Published online by Cambridge University Press

RAIM as the main method for aircraft integrity monitoring. Recent research on RAIM performance for aviation applications, for example in the framework of the Advanced RAIM (ARAIM) research effort described in Walter et al. (2008) and Blanch et al. (2013) has shown the potential for very good global system availability for specific aviation applications using multi-constellation GNSS (Blanch et al., 2007; Lee and McLauglin, 2007; FAA, 2011).

However, most RAIM algorithms require knowledge of the prior probability of fault occurrence. Further, RAIM performance is often sensitive to variations in the assumed values of this prior probability. Due to the scarcity of observed faults over the relatively short operational history of GNSS and the difficulty in developing analytical failure models for such sophisticated systems, it is not clear how to rigorously establish the probability of fault occurrence for use in RAIM algorithms. Moreover, the probability of satellite failure might evolve with satellite age. In the end it will be extremely difficult, if not impossible, to confidently specify a precise prior probability of fault occurrence. Overly optimistic values will result in misleading integrity performance predictions, and could even endanger aircraft safety when implemented for real-time detection. On the other hand, using overly conservative values will ensure conservative integrity performance predictions, but at the expense of decreased navigation availability.

Bayesian analysis is well known for its robustness to uncertainty in prior probabilities (Berger, 1985). In Bayesian analysis, the *posterior* probability of fault occurrence can be evaluated based on current measurements, an approximated prior probability of fault occurrence (Ober, 2003), and the probability density function of the fault magnitude. However, information on fault magnitude distributions is usually not available, and in this work, upper bounds on the *posterior* fault probabilities are instead sought by considering the worst-case fault magnitude. In Section 2 of this paper, a new method is developed to compute an upper bound on the *posterior* probability of a given fault hypothesis using Bayes' theorem. The penalty for the lack of information on the fault magnitude distribution will affect the tightness of the *posterior* probability bound.

In Section 3, an upper bound on integrity risk is analytically derived using the measurement-updated *posterior* probability bounds developed in Section 2. The method is illustrated using a quantitative example, which is used to demonstrate that the resulting risk assessment is robust to uncertainty in the assumed prior probabilities.

In addition, it is noted that currently most GNSS position estimators optimise accuracy (e.g., using weighted least squares estimators or Kalman filters) rather than integrity. This is true even for aviation applications that must comply with extremely stringent requirements on system integrity in order to address safety-of-life concerns. In Section 4, we introduce a Bayesian fault-tolerant position estimation (FTE) technique to optimise integrity risk instead of accuracy. The concept of using FTEs together with RAIM is not new (Pervan et al., 1998; Hwang and Brown, 2006; Lee, 2006; Blanch et al., 2012; Joerger et al., 2012). However, non-Bayesian RAIM methods for this purpose often result in complicated derivations and solutions that are difficult to obtain (ibid). Furthermore, they are subject to the same sensitivity to uncertainty prior fault probability noted earlier. The Bayesian FTE method, in contrast, can be derived analytically in a straightforward manner and is much less sensitive to prior fault probabilities. In the remainder of Section 4 the Bayesian FTE is

https://doi.org/10.1017/S0373463314000241 Published online by Cambridge University Press

then seamlessly incorporated with a fault detection algorithm developed in Pervan et al. (1998), which serves as the RAIM detection method. The test statistic adopted for fault detection is the computed system integrity risk bound, which is directly compared with the integrity risk requirement.

Continuity risk is a competing requirement (to integrity) in practical applications, including aviation applications. It is conventionally represented as a frequentist probability of monitor alarm under fault-free conditions. In order to demonstrate compliance with such a requirement, the fault-free performance of the Bayesian algorithm developed in Section 4 must be evaluated relative to the frequentist continuity risk requirement. While this is straightforward to do in principle, in practice it is extremely time consuming to precisely compute the false alarm probability. This issue is addressed in Section 5, where an efficient method suitable for real-time implementation is developed to establish an upper bound on continuity risk.

Finally, the performance of the Bayesian FTE algorithm is analysed for an example GNSS navigation system. A benchmark application, the LPV 200 aircraft precision approach (FAA, 2007), is selected for this purpose. The performance of a conventional ARAIM method is also evaluated for comparison. The simulation results demonstrate that the Bayesian FTE algorithm is robust to uncertainty in fault prior probability, while the conventional ARAIM results in much larger unaccounted for variations in integrity risk.

2. *POSTERIOR* PROBABILITY OF FAULT OCCURRENCE USING MEASUREMENTS AND BAYESIAN PROBABILITY.

In Bayesian statistics a *posterior* probability is determined based on a given prior probability and on available measurements. This *posterior* probability is conditioned upon actual measurements. The algorithm derived in Pervan et al. (1998) to compute the integrity of a position estimate using a multiple hypothesis approach for differential GPS positioning systems is extended in this work to stand-alone positioning using a Bayesian approach. The concept of using mutually exclusive multiple hypotheses has been widely adopted in recent GNSS navigation integrity research (Walter et al., 2008; Blanch et al., 2007; Lee and McLaughlin, 2007).

A set of mutually exclusive and exhaustive hypotheses (H_i, $i = 1 \ldots n_f$) is considered, where each hypothesis is associated with a specific failure mode (a particular set of faulted measurements) except the hypothesis H_0, which represents the fault-free hypothesis.

$$1 = \sum_{i=0}^{n_f} P(H_i) \tag{1}$$

where $P(H_0)$ is the prior probability for fault-free hypothesis H_0, $P(H_i)$ is the prior probability for the hypothesis H_i of the i^{th} failure mode, and n_f is the total number of hypotheses under consideration.

The measurement vector z, made of n stacked GNSS ranging signals, is expressed using the n by m ($n > m$) observation matrix G, the m by one state vector x, and the n by one nominal measurement error vector v (assumed normally distributed with zero mean) as:

$$z = Gx + v, \quad v \sim N(0, \sigma^2) \tag{2}$$

https://doi.org/10.1017/S0373463314000241 Published online by Cambridge University Press

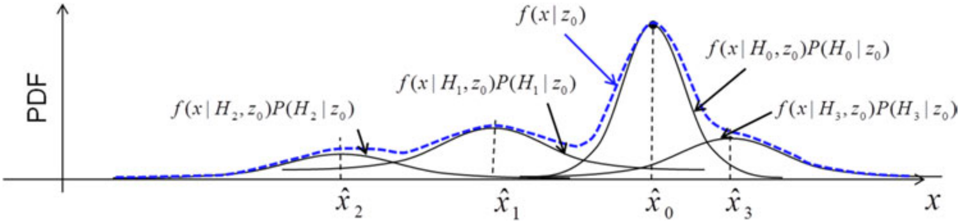

Figure 1. Illustration of the composite PDF of the true position using the multiple-hypothesis approach.

The least squares position estimate is:

$$\hat{x}_0 = (G_0^T R_0^{-1} G_0)^{-1} G_0^T R_0^{-1} z_0, \quad R_0 = [E(v_0 v_0^T)] \tag{3}$$

where the subscript 0 indicates the full-set solution (i.e., using measurements from all visible satellites), R_0 is the measurement error covariance matrix, and the m estimated states $\hat{x}_0$ are three position components and one receiver clock bias (or multiple receiver clock biases for multiple constellations).

Given the fault-free hypothesis H_0 and the full-set measurement vector z_0, the conditional probability density function (PDF) of the true position can be expressed as:

$$f(x|H_0, z_0) = N(\hat{x}_0, P_0), \quad P_0 = (G_0^T R_0^{-1} G_0)^{-1} \tag{4}$$

where P_0 is the covariance matrix of position estimate error.

For the hypothesis H_i corresponding to the i^{th} failure mode with a prior probability $P(H_i)$, a fault-free sub-set solution is obtained using the least squares estimate which excludes the i^{th} set of assumed faulty measurements:

$$\hat{x}_i = (G_i^T R_i^{-1} G_i)^{-1} G_i^T R_i^{-1} z_i, \quad R_i = [E(v_i v_i^T)] \tag{5}$$

The conditional PDF of true position under the hypothesis H_i given the sub-set measurement vector z_i can be written as:

$$f(x|H_i, z_0) = N(\hat{x}_i, P_i), \quad P_i = (G_i^T R_i^{-1} G_i)^{-1} \tag{6}$$

Because the hypotheses are mutually exclusive and exhaustive, a composite PDF for true position given all available measurements z_0 can be derived as the weighted sum of the PDFs associated with each hypothesis:

$$f(x|z_0) = \sum_{i=0}^{n_f} f(x|H_i, z_0) P(H_i|z_0) = \sum_{i=0}^{n_f} f(x|H_i, z_i) P(H_i|z_0) \tag{7}$$

where $f(x|H_i, z_0)=f(x|H_i, z_i)$ because the i^{th} set of assumed faulty measurements are not informative under H_i.

A simplified graph showing a composite PDF from the PDFs of three sub-set solutions $\hat{x}_i$ ($i=1$ to 3) and the full solution $\hat{x}_0$ is shown in Figure 1.

The $\hat{x}$ represents a single component of the estimated position vector in the figure. In the illustrative examples in this work, which are aviation examples, we will mainly focus on the vertical position coordinate, because vertical requirements are typically

https://doi.org/10.1017/S0373463314000241 Published online by Cambridge University Press

more stringent in aviation applications. However, the same methodology applies to the horizontal components of the position estimate as well.

In Equation (7), the composite PDF can be defined only if the *posterior* probability $P(H_i|z_0)$ for each hypothesis can be obtained precisely. However, for GNSS this is not possible because distributions of failure magnitudes are generally not available. An alternative approach, which we pursue in this work, is to derive an upper bound on the *posterior* probability, which will then be used to form an upper bound on integrity risk.

Using Bayes' theorem, the *posterior* probability given all available measurements z_0 can be expressed as:

$$P(H_i|z_0) = \frac{f\,(z_0|H_i)P(H_i)}{\sum_{j=0}^{n_f} f\,(z_0|H_j)P(H_j)} \tag{8}$$

Given the full-set of n measurements z_0, the information about the faults is carried only by the associated n-m by 1 parity vector p, which is defined using Equation (8.1) (Pervan et al., 1996; Sturza, 1989):

$$p = Lz_0 \tag{8.1}$$

where L is an n-m by n projection matrix. The details of how to compute matrix L and parity vector p will be discussed later.

For the moment, it is only relevant that the only part of measurement vector z_0 that is informative about the faults is more compactly expressed by the parity vector p. Therefore, this vector will be used to in place of z_0 to derive the *posterior* probability of fault occurrence:

$$P(H_i|z_0) = P(H_i|p) \quad \Rightarrow \quad P(H_i|p) = \frac{f\,(p|H_i)P(H_i)}{\sum_{j=0}^{n_f} f\,(p|H_j)P(H_j)} \tag{8.2}$$

The conditional PDF $f(p|H_j)$ can be further expanded as:

$$f\,(p|H_j) = \int_{-\infty}^{\infty} f\,(p|b_j, H_j)f_b(b_j|H_j)db_j \tag{9}$$

where $f_b(b_j|H_j)$ is the unknown conditional failure-magnitude distribution function for the j^{th} failure mode.

After substituting Equation (9) into Equation (8.2), the Bayesian *posterior* probability of hypothesis i is:

$$P(H_i|p) = \frac{\int_{-\infty}^{\infty} f\,(p|b_i, H_i)f_b(b_i|H_i)db_iP(H_i)}{\sum_{j=0}^{n_f} \int_{-\infty}^{\infty} f\,(p|b_j, H_j)f_b(b_j|H_j)db_jP(H_j)} \tag{10}$$

Since every term in Equation (10) has a positive value, an upper bound of the Bayesian *posterior* probability can be obtained by lower bounding all denominator terms by zero, except for terms corresponding to $j=0$ and $j=i$. The upper bound on the *posterior* probability for fault-free hypothesis, $i=0$, is simply one since in this special case all terms other than $j=0$ in the denominator are lower bounded by zeros.

https://doi.org/10.1017/S0373463314000241 Published online by Cambridge University Press

For values $i > 1$, Equation (10) can be upper bounded more tightly as:

$$\frac{\int_{-\infty}^{\infty} f(p|b_i, H_i) f_b(b_i|H_i) db_i P(H_i)}{\int_{-\infty}^{\infty} f(p|b_0, H_0) f_b(b_0|H_0) db_0 P(H_0) + \int_{-\infty}^{\infty} f(p|b_i, H_i) f_b(b_i|H_i) db_i P(H_i)} \geqslant P(H_i|p)$$

For the fault-free hypothesis (H_0), the failure magnitude b_0 is known to be zero. Therefore, the first integral in the denominator of the inequality above can be evaluated directly. The left-hand side of the inequality then takes the form of $w/(c+w)$, where c is a constant and w is an integral that depends on the failure magnitude distribution. This form is a monotonically ascending function in the variable w. Therefore, maximizing w will also maximize the function $w/(c+w)$. As a result, a bounding value on the *posterior* probability $P(H_i|p)$ is obtained by finding the maximum value of the integral term w:

$$\hat{P}(H_i|p) = \frac{\max\limits_{f_b, b_i} \int_{-\infty}^{\infty} f(p|b_i, H_i) f_b(b_i|H_i) db_i P(H_i)}{f(p|b_0 = 0, H_0) P(H_0) + \max\limits_{f_b, b_i} \int_{-\infty}^{\infty} f(p|b_i, H_i) f_b(b_i|H_i) db_i P(H_i)} \geqslant P(H_i|p) \quad (11)$$

Finding the maximum value of the integral term in Equation (11) involves dealing with the unknown failure magnitude distribution. Considering only single measurement faults, the parameter b_i in Equation (11) is a scalar, and the failure magnitude b_i^* which corresponds to the maximum value of the conditional PDF of the parity vector p is defined as:

$$b_i^* = \arg\max_{b_i} f(p|b_i, H_i) \quad (12)$$

The worst-case scenario for the unknown failure magnitude PDF is therefore a Dirac delta function centred at b_i^*. The resulting maximum value of the integral becomes:

$$\begin{aligned} \max_{f_b, b_i} \int_{-\infty}^{\infty} f(p|b_i, H_i) f_b(b_i|H_i) db_i &= \int_{-\infty}^{\infty} f(p|b_i, H_i) \delta_b(b_i - b_i^*|H_i) db_i \\ &= f(p|b_i^*, H_i) \end{aligned} \quad (13)$$

Substituting the above result into Equation (11), the bounding *posterior* probability can be expressed as:

$$\hat{P}(H_i|p) = \frac{f(p|b_i^*, H_i) P(H_i)}{f(p|b_0 = 0, H_0) P(H_0) + f(p|b_i^*, H_i) P(H_i)} \quad (14)$$

Equation (14) assumes the worst-case failure magnitude b_i^* defined in Equation (12) is known.

2.1. *Derivation of the worst case failure magnitude* b_i^*. Consider the general linear measurement Equation (2) under a fault condition. A failure vector b is added to Equation (2), and the equation is then normalised by pre-multiplying with the inverse square root of the measurement noise covariance matrix R. The subscript 0 in this derivation is omitted since all equations use the full set of measurements:

$$R^{-1/2} z = R^{-1/2} G x + R^{-1/2} b + R^{-1/2} v \;\Rightarrow\; z^* = G^* x + R^{-1/2} b + v^* \quad (15)$$

https://doi.org/10.1017/S0373463314000241 Published online by Cambridge University Press

The n by m ($n>m$) observation matrix G^* can be decomposed by singular value decomposition (SVD):

$$G^*_{n\times m} = U_{n\times n}\begin{bmatrix} S_{m\times m} \\ 0_{(n-m)\times m}\end{bmatrix} V^T_{m\times m} \tag{16}$$

where the n by n matrix U can be partitioned into an n by m matrix U_1 and an n by n-m matrix U_2. U_2 maps the measurements into the parity space (Pervan et al., 1996):

$$U_{n\times n} = \begin{bmatrix} U_{1,n\times m} & U_{2,n\times(n-m)}\end{bmatrix} \tag{17}$$

The parity vector p is the projection of the normalized measurements in parity space. Under fault-free conditions, the elements of p are independent and identically distributed (i.i.d.) Gaussian random variables with zero mean and unit variance. Under faulty conditions, the fault vector b causes the parity vector to have a non-zero mean, which can be expressed as:

$$p = U_2^T z^* = U_2^T R^{-1/2} b + U_2^T v^*, \quad \Rightarrow p = Lb + U_2^T v^* \tag{18}$$

where $L = {U_2}^T R^{-1/2}$, $f(p|b, H_i) = N(Lb, I_{n\text{-}m})$, and $I_{n\text{-}m}$ is the identity matrix of size n-m by n-m.

For hypothesis H_i of a fault on measurement i, we define the failure magnitude b_i of the fault vector b. The product of the matrix L and the fault vector b becomes: $Lb = L_i\, b_i$, where L_i is the i^{th} column of L. Using Equation (18), the PDF of the parity vector given hypothesis H_i can then be written as:

$$\begin{aligned} f(p|b, H_i) &= f(p|b_i, H_i) = N(L_i b_i, I_{n-m}) \\ &= \frac{1}{(2\pi)^{(n-m)/2}}\exp\left(-\frac{(p-L_i b_i)^T(p-L_i b_i)}{2}\right) \end{aligned} \tag{19}$$

For fault-free hypothesis H_0, Equation (19) becomes:

$$f(p|b_0 = 0, H_0) = \frac{1}{(2\pi)^{(n-m)/2}}\exp\left(-\frac{p^T p}{2}\right) \tag{20}$$

To maximize the conditional PDF shown in Equation (19), the exponent $(p - L_i b_i)^T(p - L_i b_i)$ must be minimised. To do this we take the partial derivative with respect to b_i and equate it to zero:

$$\frac{\partial}{\partial b_i}[(p-L_i b_i)^T(p-L_i b_i)] = 0 \;\Rightarrow\; L_i^T(p-L_i b_i) = 0 \tag{21}$$

It can be shown that the second partial derivative is always negative. Therefore, the failure magnitude b_i satisfying Equation (21) minimises the inner product and is the worst-case fault magnitude defined in Equation (12):

$$b_i^* = \arg\max_{b_i} f(p|b_i, H_i) = (L_i^T L_i)^{-1} L_i^T p \tag{22}$$

Substituting Equation (22) into Equation (19) and rearranging terms, the maximum value of the conditional PDF of the parity vector is:

$$f(p|b_i^*, H_i) = \frac{1}{(2\pi)^{(n-m)/2}}\exp\left(-\frac{p^T(I_{n-m} - L_i(L_i^T L_i)^{-1}L_i^T)p}{2}\right) \tag{23}$$

https://doi.org/10.1017/S0373463314000241 Published online by Cambridge University Press

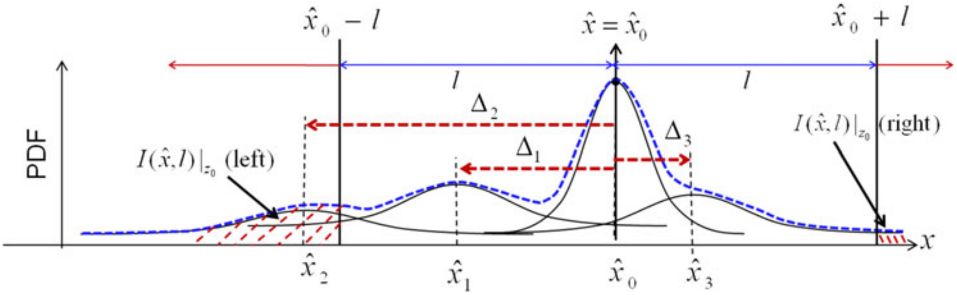

Figure 2. Illustration of the integrity risk using Bayesian approach.

Using the results from Equations (20) and (23), the bound on the *posterior* probability shown in Equation (14) is:

$$\hat{P}(H_i|p) = \frac{\exp\left(-\dfrac{p^T(I_{n-m} - L_i(L_i^T L_i)^{-1} L_i^T)p}{2}\right) P(H_i)}{\exp\left(-\dfrac{p^T p}{2}\right) P(H_0) + \exp\left(-\dfrac{p^T(I_{n-m} - L_i(L_i^T L_i)^{-1} L_i^T)p}{2}\right) P(H_i)} \tag{24}$$

3. ROBUSTNESS OF INTEGRITY EVALUATION USING BAYESIAN APPROACH.

From the Bayesian point-of-view, integrity risk is defined as the conditional probability, given the measurements, that the state estimation error, δx, exceeds a prescribed limit $\pm l$ (often called an alert limit):

$$I_{risk}|_z \equiv P(|\delta x| > l|z) \tag{25}$$

The Bayesian integrity risk is a function of the composite PDF of the true position x in Equation (7), the alert limit, and the choice of position estimate $\hat{x}$ used for navigation. We start by using the full-set solution $\hat{x}_0$ as the navigation estimate. As illustrated in Figure 2, the integrity risk is the cumulative probability of the true position being outside the interval of length $2l$ centred at the navigation solution $\hat{x}_0$. It can be expressed as the sum of the tail-probability of each hypothesis weighted by the *posterior* probability of occurrence of each hypothesis given the measurements:

$$I_{risk}(\hat{x}_0, l)|_{z_0} = P(|x - \hat{x}_0| > l|z_0) = \sum_{i=0}^{n_f} P(|x - \hat{x}_0| > l|H_i, z_0) P(H_i|z_0) \tag{26}$$

The difference between the i^{th} sub-set solution and the full-set solution is defined as the i^{th} solution separation value Δ_i: $\Delta_i \equiv \hat{x}_i - \hat{x}_0$. Assuming zero-mean, normally distributed measurement noise, the tail-probability of each hypothesis can be evaluated as a sum of complementary error functions:

$$\begin{aligned} P(|x - \hat{x}_0| > l|H_i, z_0) &= \int_{-\infty}^{\hat{x}_0 - l} f(x|H_i, z_0)dx + \int_{\hat{x}_0 + l}^{\infty} f(x|H_i, z_0)dx \\ &= \frac{1}{2}\left(\operatorname{erfc}\left[\frac{l - \Delta_i}{\sqrt{2}\sigma_i}\right] + \operatorname{erfc}\left[\frac{l + \Delta_i}{\sqrt{2}\sigma_i}\right]\right) \end{aligned} \tag{27}$$

https://doi.org/10.1017/S0373463314000241 Published online by Cambridge University Press

The Bayesian integrity risk using the full-solution can then be written as:

$$\begin{aligned} I_{risk}(\hat{x}_0, l)|_{z_0} &= \frac{1}{2}\sum_{i=0}^{n_f}\left\{\mathrm{erfc}\left[\frac{l-\Delta_i}{\sqrt{2}\sigma_i}\right] + \mathrm{erfc}\left[\frac{l+\Delta_i}{\sqrt{2}\sigma_i}\right]\right\}P(H_i|z_0) \\ &= \frac{1}{2}\sum_{i=0}^{n_f}\left\{\mathrm{erfc}\left[\frac{l-\Delta_i}{\sqrt{2}\sigma_i}\right] + \mathrm{erfc}\left[\frac{l+\Delta_i}{\sqrt{2}\sigma_i}\right]\right\}P(H_i|p) \end{aligned} \tag{28}$$

It is important to note that, as shown in Chan and Pervan (2010), the solution separation values Δ_i can be directly obtained from the parity vector p as a scaled vector projection of p on the i^{th} row of U_2, which is the same direction as the fault mode L_i:

$$[\,\Delta_{i,x} \quad \Delta_{i,y} \quad \Delta_{i,z} \quad \Delta_{i,clk}\,]^T = -(I - P_0 g_i g_i^T)^{-1} P_0 g_i r_i, \qquad r_i = U_2(i,:)p \tag{28.a}$$

where $\Delta_{i,x}$, $\Delta_{i,y}$, $\Delta_{i,z}$, $\Delta_{i,clk}$ are the x, y, z and receiver clock bias components in the i^{th} solution separation vector, g_i is the i^{th} column in the observation matrix G, r_i is the i^{th} residual element obtained by projecting the parity vector onto the i^{th} fault mode which is represented by the i^{th} row of U_2 matrix (U_2 $(i,:)$).

Equation (28) is the Bayesian system integrity risk. As noted earlier, the *posterior* probability of each hypothesis' given measurements cannot be precisely evaluated when the failure-magnitude distribution function is unknown. Instead, the *posterior* bounds in Equations (8) to (24) are used to obtain an upper bound on the Bayesian integrity risk:

$$\hat{I}_{risk}(\hat{x}_0, l)|_{z_0} = \frac{1}{2}\sum_{i=0}^{n_f}\left\{\mathrm{erfc}\left[\frac{l-\Delta_i}{\sqrt{2}\sigma_i}\right] + \mathrm{erfc}\left[\frac{l+\Delta_i}{\sqrt{2}\sigma_i}\right]\right\}\hat{P}(H_i|p) \quad \geqslant \quad I_{risk}(\hat{x}_0, l)|_{z_0} \tag{29}$$

One particularly interesting property of the integrity risk bound Equation (29), which is inherited from Bayesian approach, is its relative insensitivity to prior probabilities (also known as *posterior* robustness (Berger, 1985)). A frequentist approach for system integrity evaluation uses a fixed prior probability for each assumed hypothesis. Proving that these fixed values upper bound the actual prior probabilities is typically not possible. The Bayesian approach mitigates the issue by generating a *posterior* probability update based on current time measurements.

We illustrate the Bayesian approach through an example of positioning using a nominal GPS constellation. The constellation used is adopted from earlier ARAIM research described by the GNSS Evolutionary Architecture Study (GEAS) in FAA (2011). We consider a single satellite geometry epoch at one location, in which six satellites (SVs) are in view. In this case, the parity space is two-dimensional and is easy to represent graphically. Measurement error was modelled as a function of elevation based on the GEAS/ARAIM error models in Lee and McLaughlin (2007).

Figure 3 shows the parity space for this example and the failure mode lines for each fault mode hypothesis (only single satellite failures are considered). The failure mode direction for satellite i can be obtained by replacing the fault vector b in Equation (18) with $L_i\,b_i$. The direction of the blue dashed arrow is arbitrarily picked as an example (actual) parity vector direction; the parity vector magnitude is made to vary linearly to illustrate the variation of the *posterior* probability bound. The resulting *posterior* probability bounds for each hypothesis are shown in Figure 4 as functions of the parity

https://doi.org/10.1017/S0373463314000241 Published online by Cambridge University Press

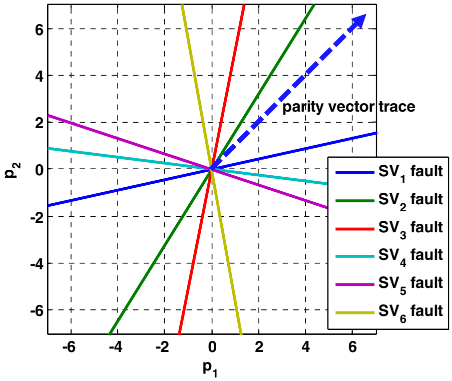

Figure 3. Parity space and fault modes.

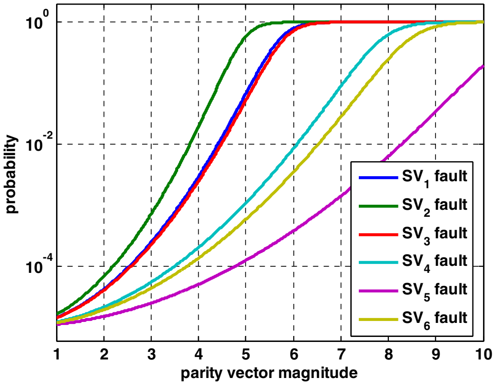

Figure 4. Bayesian *posterior* probability bounds.

vector magnitude. A prior probability $P(H_i)=1\times10^{-5}$, for all i, was used to generate the results. The figure shows that the larger the magnitude of a parity vector, the more likely it is to be the result of a fault. Figure 5 illustrates one specific parity vector p and two associated worst-case fault magnitudes for single SV 5 and 6 fault modes derived using Equation (22).

Figure 6 shows the Bayesian integrity risk bounds from Equation (29) (the z axis is logarithmic in scale) corresponding to all parity vectors (the p_1 and p_2 axes) for the example geometry using a 35 metre vertical alert limit ($l=\pm35$ m). The figure illustrates that the integrity risk bound is convex in a valley shape. The horizontal blue curve in the middle of the valley represents an example constant integrity risk contour, which is also shown in Figure 7. The integrity risk value is $8{\cdot}7\times10^{-8}$ in this example. (The reason for the choice of this particular value will become evident later in Section 5.) In addition, Figure 7 shows two other constant integrity risk contours (red and magenta) associated with the same integrity risk ($8{\cdot}7\times10^{-8}$), but respectively evaluated with ten and 100 times larger prior probabilities (1×10^{-4} and 1×10^{-3}). In the figure, the Bayesian integrity risk bound contours change only slightly with large variations in prior probability. This visually illustrates that the Bayesian integrity risk

https://doi.org/10.1017/S0373463314000241 Published online by Cambridge University Press

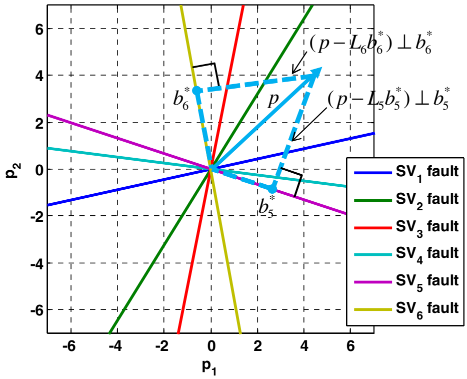

Figure 5. Illustration of a specific parity vector p.

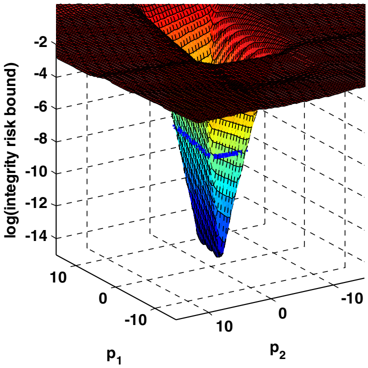

Figure 6. Bayesian integrity risk bounds in parity space.

bound is not sensitive to prior probability variation. The significance of the robustness of the Bayesian integrity risk to prior probability will become compelling in Section 5 when system performance using traditional RAIM will be compared to the Bayesian approach.

4. FAULT-TOLERANT POSITION ESTIMATION AND BAYESIAN RAIM DETECTION.

The Bayesian integrity risk bound derived in the previous section uses a least-squares solution $\hat{x}_0$ as navigation solution, but this is not necessarily the only choice. In fact, Equation (26) defines the Bayesian integrity risk for any arbitrary position estimate $\hat{x}$:

$$I_{risk}(\hat{x}, l)|_{z_0} = P(|x - \hat{x}| > l|z_0) = \sum_{i=0}^{n_f} P(|x - \hat{x}| > l|H_i, z_0)P(H_i|z_0) \tag{30}$$

Following the derivation in Pervan et al. (1998), an arbitrary position estimate can be expressed as an offset from the full-set least-squares solution: $\Delta \equiv \hat{x} - \hat{x}_0$. The Bayesian integrity risk bound for an arbitrary position estimate can be derived

https://doi.org/10.1017/S0373463314000241 Published online by Cambridge University Press

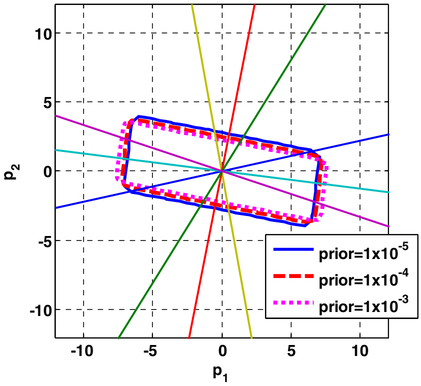

Figure 7. Bayesian integrity risk bound contours in parity space.

similarly to Equations (27)–(29) to be:

$$\begin{aligned}\hat{I}_{risk}(\hat{x}, l)|_{z_0} &= \frac{1}{2}\sum_{i=0}^{n_f}\left\{\text{erfc}\left[\frac{l-(\Delta_i-\Delta)}{\sqrt{2}\sigma_i}\right]+\text{erfc}\left[\frac{l+(\Delta_i-\Delta)}{\sqrt{2}\sigma_i}\right]\right\}\hat{P}(H_i|p)\\ &\geqslant I_{risk}(\hat{x}, l)|_{z_0}\end{aligned} \tag{31}$$

Given the alert limit l and current measurements, the Bayesian integrity risk bound in Equation (31) is only a function of the offset Δ. Therefore, we may choose Δ to minimize the Bayesian integrity risk bound. This results in a 'fault-tolerant' position estimate (FTE): $\hat{x}_{FTE} = \Delta + \hat{x}_0$.

$$\begin{aligned}\hat{I}_{risk}(\hat{x}_{FTE}, l)|_{z_0} &\equiv \min_{\hat{x}} \hat{I}_{risk}(\hat{x}, l)|_{z_0}\\ &= \min_{\Delta}\frac{1}{2}\sum_{i=0}^{n_f}\left\{\text{erfc}\left[\frac{l-(\Delta_i-\Delta)}{\sqrt{2}\sigma_i}\right]+\text{erfc}\left[\frac{l+(\Delta_i-\Delta)}{\sqrt{2}\sigma_i}\right]\right\}\hat{P}(H_i|p)\end{aligned} \tag{32}$$

The derivation of the FTE has been shown in Pervan et al. (1998), and the result is expressed below:

$$\begin{aligned}&\frac{d}{d\Delta}\left\{\frac{1}{2}\sum_{i=0}^{n_f}\left\{\text{erfc}\left[\frac{l-(\Delta_i-\Delta)}{\sqrt{2}\sigma_i}\right]+\text{erfc}\left[\frac{l+(\Delta_i-\Delta)}{\sqrt{2}\sigma_i}\right]\right\}\hat{P}(H_i|p)\right\}=0\\ &\Rightarrow \sum_{i=0}^{n_f}\frac{\hat{P}(H_i|p)}{\sigma_i}\left\{\exp\left[-\left(\frac{l-(\Delta_i-\Delta)}{\sqrt{2}\sigma_i}\right)^2\right]+\exp\left[-\left(\frac{l+(\Delta_i-\Delta)}{\sqrt{2}\sigma_i}\right)^2\right]\right\}=0\end{aligned} \tag{33}$$

The FTE solution Δ cannot be expressed in closed form, but it can be obtained numerically with great efficiency. Therefore, a real-time implementation is feasible. Figure 8 shows numerical results of the Bayesian integrity risk bound for the vertical positioning component using the example from the previous section. In this figure, the Bayesian integrity risk bound resulting from the FTE is about +3·2 m off the least squares estimate, but its integrity risk is two orders of magnitude lower.

https://doi.org/10.1017/S0373463314000241 Published online by Cambridge University Press

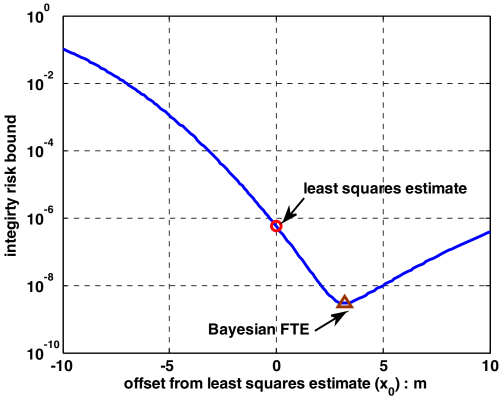

Figure 8. The Bayesian integrity risk bounds for different position estimate.

The fault detection algorithm for this Bayesian approach is a direct comparison between two values: the computed Bayesian integrity risk bounds, noted as I_{comp}, and a detection threshold using the allocated integrity risk requirement, noted as I_{req}.

$$I_{comp} \equiv \hat{I}_{risk}(\hat{x}, l)|_{z_0}, \quad \text{detection} : I_{comp} \geqslant I_{req}, \quad \text{no-detection} : I_{comp} < I_{req} \tag{34}$$

This detection mechanism is different from conventional RAIM methods, which normally set detection thresholds based on a continuity requirement. Using this Bayesian detection algorithm, system continuity is yet to be evaluated. This will be addressed in Section 5.

5. CONTINUITY AND EXAMPLE SYSTEM PERFORMANCE EVALUATION.

For civil aviation applications, continuity risk is defined as the probability of interrupting an aircraft operation that has already been initiated. It is directly related to the false alarm rate of the fault detection algorithm. To illustrate the connection between fault detection performance and continuity requirement using the Bayesian approach, an example application, LPV-200 precision approach (FAA, 2007), is considered.

LPV-200 precision approach has been wildly studied for the next generation GNSS. As in the example in Section 3, measurement error models are adopted from GEAS/ ARAIM (FAA, 2011), with exception of the bias errors treated in that prior work, which are excluded here for simplicity. Further, only the vertical position error, which has the most stringent requirements in LPV-200 performance, is considered.

The simulation parameters used in Section 3 are implemented again for one example geometry with six satellites in view at the same example location. For the purpose of the example, a continuity risk requirement of 4×10^{-6} and an integrity risk requirement of $8{\cdot}7 \times 10^{-8}$, with an associated 35 m alert limit, are allocated to the vertical positioning component from the total LPV-200 requirements. To better understand the methods for continuity risk evaluation, the least-squares position estimate is first used and only single-satellite-failure modes are considered. Then, the same methods are extended to the Bayesian FTE solution for system performance evaluation.

https://doi.org/10.1017/S0373463314000241 Published online by Cambridge University Press

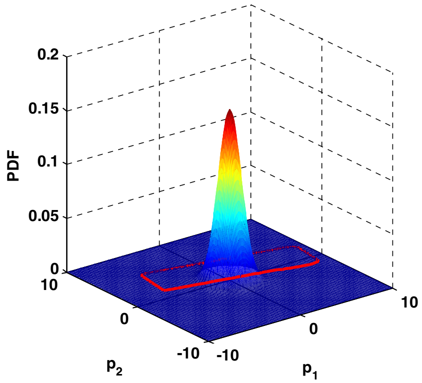

Figure 9. Probability density in parity space under fault-free hypothesis.

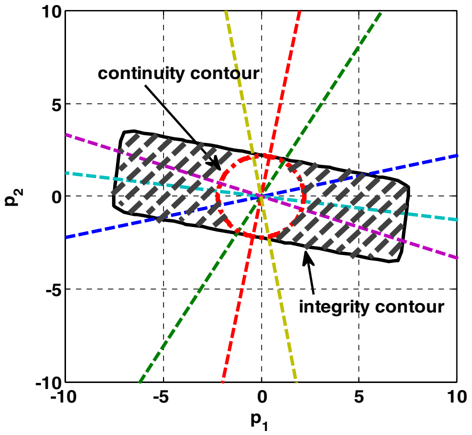

Figure 10. Computed continuity risk (2×10^{-4}) using circular continuity contour.

Figure 9 shows the *a priori* joint PDF of the parity vector under fault-free conditions. The integrity risk contour (red line contour) corresponding to *posterior* Bayesian integrity risk bound of $8{\cdot}7 \times 10^{-8}$ is also shown. The contour was evaluated using the above-mentioned example with 1×10^{-5} prior probabilities for all fault hypotheses. It represents the detection boundary in parity space (a parity plane in this example) for the Bayesian detection algorithm. If a parity vector falls outside the contour ($I_{comp} \geqslant I_{req}$), detection is declared and the aircraft approach is interrupted. Therefore, the false alarm contribution to continuity risk is the cumulative probability that the parity vector, under fault-free conditions, falls outside the detection contour. Precisely computing this accumulated probability is challenging, because the contour of constant integrity risk is a smooth and continuous enclosed curve (as seen in Figure 9), which cannot be represented analytically in closed form. This becomes even more challenging when the dimension of the parity space becomes higher (i.e. when more visible satellites are available). A potential method to solve the issue was presented in Pervan et al. (1998) and Chan and Pervan (2010), and

https://doi.org/10.1017/S0373463314000241 Published online by Cambridge University Press

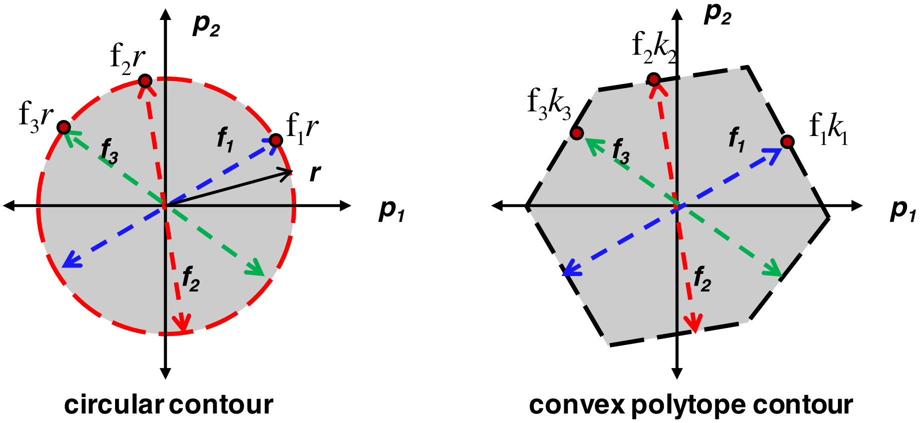

Figure 11. Different continuity contours in parity space.

one of them is briefly reviewed below. Then, a new more effective method is developed.

The cumulative probability outside a circular contour in parity space can be easily computed using the chi-squared cumulative density function (CDF). Continuity requirements are guaranteed to be met if the largest circular contour that can be inscribed within the actual detection contour has a computed continuity risk equal to or smaller than the required continuity risk (Chan and Pervan, 2010). However, as Figure 10 illustrates, this method of evaluating continuity risk can be very conservative (because the black-dashed areas in Figure 10 are not accounted for using this method). Another less conservative approach for evaluating the continuity contour uses a convex polytope contour instead of a circle. Figure 11 shows a circular contour and a convex polytope contour side by side. The radius r of the circular contour can be computed using the chi-squared CDF to meet the continuity requirement. Also shown in the figure are f_1, f_2 and f_3, which represent the unit vectors of each fault mode. (For clarity, only three fault hypotheses are assumed in this illustration.) The convex polytope is defined by a set of straight-line segments perpendicular to the fault mode lines. The specific line segments are chosen to intersect with the fault mode lines at distances $\pm k_1$, $\pm k_2$ and $\pm k_3$ from the origin. The intersection points on the polytope boundary contour, $\pm k_1 f_1$, $\pm k_2 f_2$ and $\pm k_3 f_3$, are called boundary points, and they will be used to bound continuity risk. Although the continuity risk of a convex polytope contour is not trivial to compute either, a bound can easily be found. If C is defined as an event where the parity vector lies inside a convex polytope contour, it is shown in the Appendix that the continuity risk is bounded by:

$$\hat{P}(p \in \bar{C}|H_0) = \sum_{i=1}^{n_f} P(|a_i| > k_i|H_0) \geqslant P(p \in \bar{C}|H_0) \tag{35}$$

where a_i is the magnitude of the projection on the fault mode direction from a parity vector. Therefore it is a normally distributed random variable with a unity standard deviation and zero mean under H_0.

https://doi.org/10.1017/S0373463314000241 Published online by Cambridge University Press

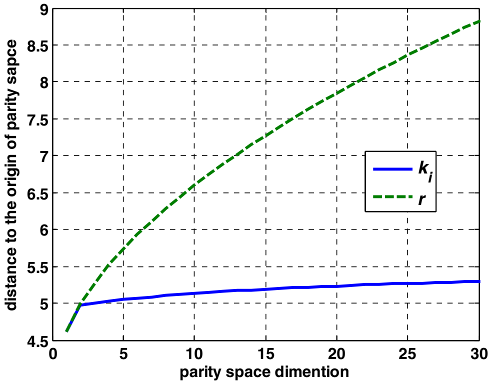

Figure 12. Distance to the origin of parity space for two continuity contours.

For our current purpose, the boundary points are specifically selected to have equal distances to the origin ($k_1 = k_2 = \ldots = k_i$) by allocating the required continuity risk evenly on each fault mode.

Computing continuity risk using the convex polytope contour is less conservative than using a circular continuity contour. The reason is that the corners of a convex polytope extend the circumscribed area beyond that of a circular contour, which ultimately provides a tighter bound on the continuity risk. This reduction in the continuity risk bound improves significantly when the dimension of the parity space increases, i.e., with a larger number of redundant satellites. Figure 12 shows the numerical results in this respect using evenly-allocated continuity for a total 4×10^{-6} continuity risk. The y-axis in the figure is the minimum magnitude of the parity vector along each fault mode that meets the continuity risk requirement using each of the two methods. The x-axis is the number of redundant satellites. To meet the continuity requirement, the *posterior* Bayesian integrity risks associated with all parity vectors with these lengths must not exceed the integrity risk requirement; otherwise the likelihood of fault-free detection will be too high. However, the bigger the magnitudes of these parity vectors become, the higher the resulting *posterior* integrity risk they have. Therefore, to achieve the same integrity risk using either method (i.e. both continuity contours inscribed within the detection contour), the computed fault free alarm probability using the convex polytope will be relatively much lower as the number of redundant satellites increases.

In addition, the convex polytope contour also offers flexibility in varying boundary points along each fault mode to more closely resemble the actual detection surface contour. In other words, the continuity risk can be allocated by individually selecting k_i for each fault mode in Equation (35). However, it should be noted that in most example ARAIM cases that we evaluated, the resulting continuity improvement is typically small.

In practice, the convex polytope contour is first defined to achieve the required continuity risk. Then, it must be determined whether the Bayesian integrity risk bound meets the given integrity risk requirement at all points within the contour. This can be efficiently done by evaluating the risk bound on the polytope contour itself. Because the Bayesian integrity risk bound is a convex function (as shown in Figure 6), the maximum value of Bayesian integrity risk bound must fall on the contour.

https://doi.org/10.1017/S0373463314000241 Published online by Cambridge University Press

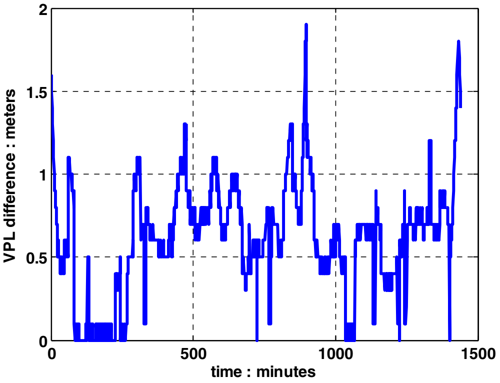

Figure 13. VPL system performance difference for two different continuity evaluation methods.

Moreover, again because of the convexity of the function, one of the two end points of each segment of the contour (i.e., the vertices of the polytope) will have risk bound larger than or equal to the risk bounds at points within the segment (Luenberger, 2003). Therefore, only the vertices of the given convex polytope are needed to evaluate the Bayesian integrity risk bounds for the whole continuity counter. The total number of risk bound evaluation points can be further reduced to half because the integrity contour is symmetric with respect to the origin of parity space. A numerical demonstration of evaluating integrity risk bounds along the continuity contour is illustrated in the Appendix.

A Protection Level (PL) is the minimum interval *l* (see Figure 2) which meets the required integrity and continuity risks. The smaller the Vertical Protection Level (VPL), the better the system performance is. In Figure 13, the VPL differences are generated over 24 hours at the previous example location by subtracting the VPLs of the convex polytope method from the VPLs of the circular contour method. It is clear in the figure that the convex polytope method performs better (smaller VPLs resulting in positive VPL difference).

The ARAIM algorithm uses a fixed set of prior probabilities for each hypothesis, but the validity of any chosen value for prior probability is often debatable. In the following example four possible values are considered: 1×10^{-2}, 1×10^{-3}, 1×10^{-4} and 1×10^{-5}. VPLs for the Bayesian FTE method are compared to those obtained using the baseline ARAIM algorithm described in FAA (2011). Simulations are performance at one location for 24 hours using a 24-minus-1 SV GPS constellation (the GPS Standard Positioning Service Performance Standard (US DOD, 2001) depleted by one satellite). Figure 14 illustrates the VPL variations for both methods using the actual prior probabilities of 1×10^{-2}, 1×10^{-3}, 1×10^{-4} relative to an assumed value of 1×10^{-5}. The deviations are shown in terms of the ratio of VPLs relative to the 1×10^{-5} case. Because the Bayesian FTE algorithm is less sensitive to prior probability variations, for clarity only relative VPLs corresponding to the 1×10^{-2} prior probability case are shown (this is the largest deviation from the assumed value, 1×10^{-5}).

Figure 15 shows the same simulation using two constellations: a 24-minus-1 SV GPS constellation and a 27-minus-1 SV Galileo constellation (Zandbergen et al., 2004). It is evident from both figures that the actual VPL values using the Bayesian

https://doi.org/10.1017/S0373463314000241 Published online by Cambridge University Press

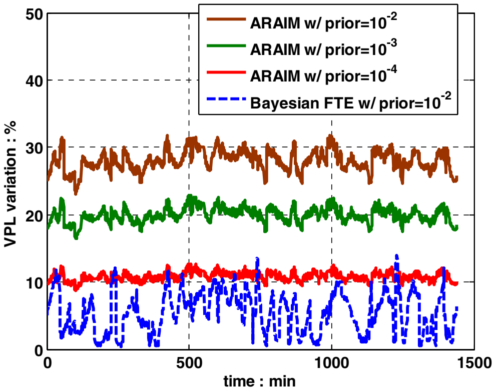

Figure 14. VPL variations with different prior probabilities for single constellation.

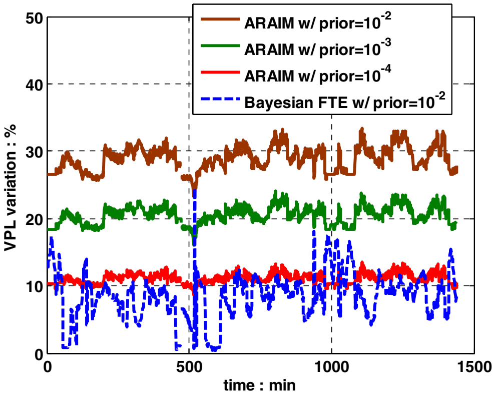

Figure 15. VPL variations with different prior probabilities for dual constellation.

FTE method are higher than the presumed values by only 10% or less most of the time, even if the actual prior probability value is 1000 times larger than what was assumed (1×10^{-5}). In contrast, the ARAIM VPLs increase approximately in proportion to the order of prior probability. This example illustrates that the Bayesian FTE is more robust to lack of knowledge of prior probability.

Robustness of the Bayesian method to the prior probability uncertainty has two meanings in terms of the system performance. Firstly, protection level robustness can further help ensure the validity of system availability evaluations (from a performance prediction point of view). To illustrate this, one example geometry is selected from the dual constellation case above for a user location near Chicago's O'Hare airport. For an LPV-200 aircraft approach, the vertical alert limit (VAL) is 35 m. Figure 16 shows variations in VPL compared to VAL for different prior probabilities. Both Bayesian approaches (one using the all-in-view position estimate as the navigation solution and the other using FTE) show that VPL variations are much less pronounced than the ARAIM case. Further, the Bayesian FTE algorithm provides extra performance improvement (smaller VPLs). The general inference is that the relative insensitivity of

https://doi.org/10.1017/S0373463314000241 Published online by Cambridge University Press

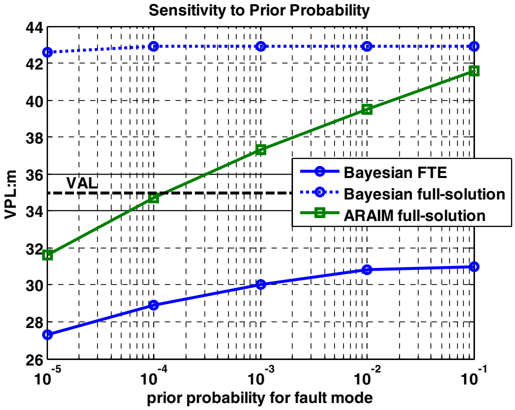

Figure 16. Demonstration of VPL variation due to prior probability.

VPL variation will therefore lead to lower system availability degradation if prior probabilities are increased.

Secondly, satellite fault probabilities may vary over time, due to aging or other reasons, so the underlying probability of satellite fault may eventually become larger than the assumed value in the ARAIM algorithm. In this scenario the aircraft-computed VPLs will be smaller than the actual VPLs, which is a potential integrity hazard.

6. CONCLUSION.

RAIM-type detection methods will be an important contributor to navigation system integrity in the near future with the advent of modernized and multi-constellation GNSS. However, most current RAIM methods rely on a fixed set of assumed prior fault probabilities. These prior probabilities are difficult to determine (and even more difficult to certify for aviation applications). They may even change over time for individual satellites, depending on satellite age and health history. In this work, Bayesian analysis was used to generate *posterior* fault probability bounds by updating the prior probabilities using current measurements. It was shown how this leads to an integrity monitoring method that is more robust to lack of knowledge in prior probabilities relative to existing, state-of-the-art Advanced RAIM (ARAIM) algorithms. The specific contributions of the paper are briefly outlined below.

A bound on the *posterior* probability was derived and used to define a bound on Bayesian system integrity risk. Using these results, a Bayesian detection algorithm was developed and a fault-tolerant position estimator (FTE) was derived.

It was noted that the main challenge in using a Bayesian approach for integrity monitoring is that the fault-free alarm probability (continuity risk) is difficult to precisely compute. In response a new, computationally efficient method was developed to obtain a tight upper bound on continuity risk.

System performance using the new Bayesian FTE algorithm was analysed by evaluating protection level variations for an example aircraft approach application. It was shown that the performance of the Bayesian FTE algorithm is more robust to the prior probability variations than state-of-the-art Advanced RAIM algorithms.

https://doi.org/10.1017/S0373463314000241 Published online by Cambridge University Press

ACKNOWLEDGMENT

The authors would like to express their appreciation to the Federal Aviation Administration for supporting this work. They are also grateful to their colleagues in the Navigation Laboratory at the Illinois Institute of Technology for their valuable advice.

REFERENCES

Berger, J.O. (1985). *Statistical decision theory and Bayesian analysis*, Springer.

Blanch, J., Ene, A., Walter, T. and Enge, P. (2007). An Optimized Multiple Hypothesis RAIM Algorithm for Vertical Guidance. ION *GNSS 20th International Technical Meeting of the Satellite Division*, Fort Worth, TX, 2924–2933.

Blanch, J., Walter, T. and Enge, P. (2012). Optimal Positioning for Advanced RAIM. *Proceeding of ION ITM*, Newport Beach, CA, 1624–1647.

Blanch, J., Walter, T., Enge, P., Wallner, S., Amarillo Fernandez, F., Dellago, R., Ioannides, R., Hernandes, I.F., Belabbas, B., Spletter, A. and Rippl, M. (2013). Critical Elements for a Multi-Constellation Advanced RAIM. *NAVIGATION*, **60**(1), 53–69.

Brown, R.G. (1996). Receiver Autonomous Integrity Monitoring. *Global Positioning System: Theory and Applications*, Vol. **II**, 143–165.

Chan, F.-C. and Pervan, B. (2010). A Practical Approach to RAIM-based Fault-Tolerant Position Estimation. *Proceedings of the 23rd International Technical Meeting of The Satellite Division of the Institute of Navigation (ION GNSS 2010)*, Portland, OR, 3181–3190.

FAA. (2007). *Program Requirements for the Wide Area Augmentation System (WAAS)*, FAA doc. WAAS070030, Jun. 5 2007.

FAA. (2011). Phase II of the GNSS Evolutionary Architecture Study. FAA report, Feb. 2011. http://www.faa.gov/about/office_org/headquarters_offices/ato/service_units/techops/navservices/gnss/library/documents/media/GEASPhaseII_Final.pdf

Frank, R. and Weston, M. (1997). A survey of Venn diagrams. *Electronic Journal of Combinatorics*. http://www.combinatorics.org/files/Surveys/ds5/VennEJC.html

Hwang, P. and Brown, R.G. (2006). RAIM FDE Revisited: A new Breakthrough in Availability Performance With NIORAIM (Novel Integrity-Optimized RAIM). *NAVIGATION*, **53**(1), 654–665.

Joerger, M., Chan, F.-C., Langel, S. and Pervan, B. (2012). RAIM Detector and Estimator Design to Minimize the Integrity Risk. *ION GNSS 25th International Technical Meeting of the Satellite Division*, Nashville, TN, 2785–2807.

Lee, Y.C. and McLaughlin, M.P. (2007). Feasibility Analysis of RAIM to Provide LPV-200 Approaches with Future GPS. *ION GNSS 20th International Technical Meeting of the Satellite Division*, Fort Worth, TX, 2898–2919.

Luenberger, D.G. (2003). *Linear and nonlinear programming*. Springer, 198.

Ober, P.B. (2003). Integrity Predication and Monitoring of Navigation Systems. PhD Dissertation, TU Delft, 93–99.

Parkinson, B.W. and Axelrad, P. (1988). Autonomous GPS Integrity Monitoring Using the Pseudorange Residual. *NAVIGATION*, **35**(2), 225–274.

Pervan, B., Lawrence, D.G., Cohen, C.E. and Parkinson, B.W. (1996). Parity Space Methods for Autonomous Fault Detection and Exclusion using GPS Carrier Phase. *IEEE 1996 Position Location and Navigation Symposium*, 649–656.

Pervan, B., Pullen, S. and Christie, J. (1998). A Multiple Hypothesis Approach to Satellite Navigation Integrity. *NAVIGATION*, **45**(1), 61–84.

Sturza, M.A. (1989). Navigation System Integrity Monitoring Using Redundant Measurements. *NAVIGATION*, **35**(4), 483–502.

US DOD. (2001). *Global positioning system standard positioning service performance standard.* Assistant secretary of Defense for Command, Control, Communications, and Intelligence.

Walter, T., Enge, P., Blanch, J. and Pervan, B. (2008). Worldwide Vertical Guidance of Aircraft Based on Modernized GPS and New Integrity Augmentations. *Proceedings of the IEEE Special Issue on Aviation Information Systems*, **96**(12), 1918–1935.

https://doi.org/10.1017/S0373463314000241 Published online by Cambridge University Press

Young, C.L. (2006). A New Improved RAIM Method Based on the Optimally Weighted Average Solution (OWAS) Under the Assumption of a Single Fault. *Proceedings of the ION National Technical Meeting*, Monterey, CA, 574–586.

Zandbergen, R., Dinwiddy, S., Hahn, J., Breeuwer, J. and Blonski, D. (2004). Galileo Orbit Selection. *Proceedings of the 17th International Technical Meeting of the Satellite Division of The Institute of Navigation* (*ION GNSS 2004*), Long Beach, CA, 616–623.

APPENDIX

PROOF OF CONVEX POLYTOPE BOUND FOR CONTINUITY RISK EVALUATION. For clarity of explanation, the same convex polytope with three fault modes in Figure 11 is used and displayed in Figure A-1. Three unit direction vectors associated with three fault modes are defined as f_1, f_2 and f_3. Three random variables can be defined as the magnitudes of the projection on three fault-mode directions from a parity vector:

$$a_1 \equiv f_1^T p, \quad a_2 \equiv f_2^T p, \quad a_3 \equiv f_3^T p \tag{A.1}$$

Under fault-free conditions, the probability that a parity vector falls inside the convex polytope contour (we call this 'event C') can be expressed as:

$$P(p \in C|H_0) = 1 - P(p \in \bar{C}|H_0) \tag{A.2}$$

where

$$P(p \in \bar{C}|H_0) = P(|a_1| \geqslant k_1 \text{ or } |a_2| \geqslant k_2 \text{ or } |a_3| \geqslant k_3|H_0) \tag{A.3}$$

which is the continuity risk. Using the Venn diagram (Frank and Weston, 1997), it is easily observed that the continuity risk can be bounded as follows:

$$\begin{aligned} P(p \in \bar{C}|H_0) &\leqslant P(|a_1| \geqslant k_1|H_0) + P(|a_2| \geqslant k_2|H_0) + P(|a_3| \geqslant k_3|H_0) \\ &\equiv \hat{P}(p \in \bar{C}|H_0) \end{aligned} \tag{A.4}$$

Using the same example as in Section 3, it is easy to numerically demonstrate that the vertices of the polytope will correspond to the maximum Bayesian integrity risk bound along the polytope contour. A convex ploytope contour is first generated using evenly allocated continuity risks; it is shown in Figure A-2. Sample points are taken on the six contour line segments densely with small incremental steps, which include all the vertices and the boundary points, starting at p_s and progressing in a counter-clockwise direction until p_e. Due to the symmetry of the polytope and the system integrity risk bound, only half of the continuity contour needs to be considered. The corresponding solution separations for each sampled parity vector can be generated using the mapping function in Equation (28.a), and the results substituted into Equation (28) to obtain the Bayesian integrity risk bounds. Figure A-3 shows these integrity risk bounds for the sampled parity vectors along the contour. In the figure, the x axis shows the distance travelled along the contour from the starting vector p_s and the y axis shows the associated probabilities (Bayesian integrity risk bounds). The marked points represent the vertices and boundary points on the contour. It can be easily seen that the maximum Bayesian system integrity risk bound is on segment three (red line segment). It is also evident that all points on segment three have

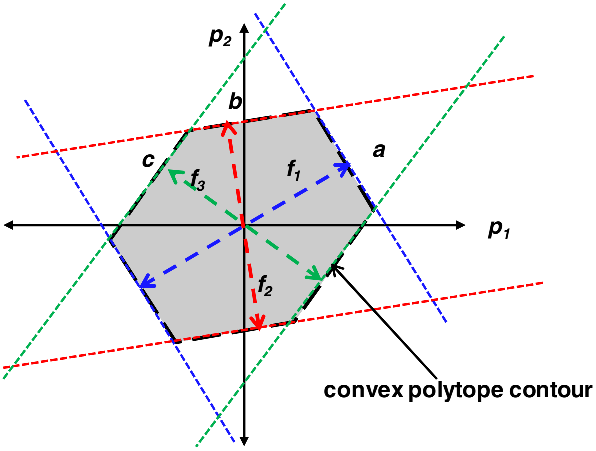

Figure A-1. Convex polytope continuity contour in parity space.

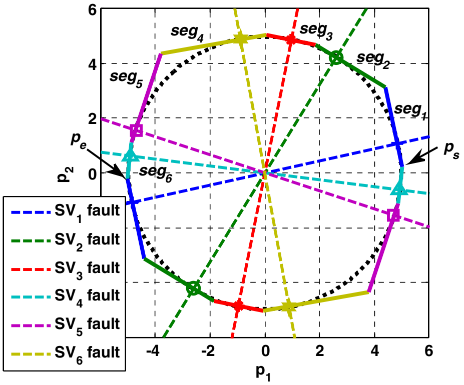

Figure A-2. Numerical simulation of a convex polytope contour.

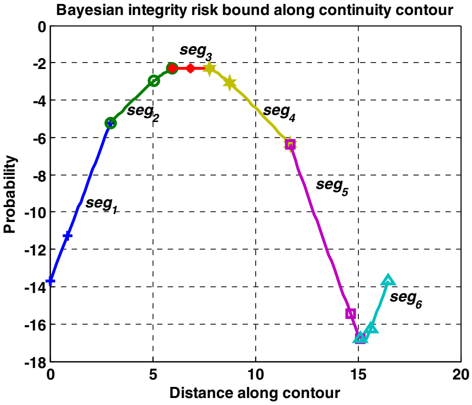

Figure A-3. Bayesian integrity risk bounds on the convex polytope contour.

https://doi.org/10.1017/S0373463314000241 Published online by Cambridge University Press

essentially the same probability values because the third fault mode is the dominant fault; in particular, this example demonstrates that the vertices of the segment three have risk bounds equal to the risk bounds at points within the segment. This numerical example demonstrates the method of evaluating the Bayesian integrity risk bound for the given continuity contour described in Section 5.

https://doi.org/10.1017/S0373463314000241 Published online by Cambridge University Press